

Quartz preferred orientation in naturally deformed mylonitic rocks (Montalto shear zone–Italy): a comparison of results by different techniques, their advantages and limitations

Eugenio Fazio¹  · Rosalda Punturo¹ · Rosolino Cirrincione¹ · Hartmut Kern² · Antonino Pezzino¹ · Hans-Rudolf Wenk³ · Shalini Goswami⁴ · Manish A. Mamtani⁴

Received: 10 October 2016 / Accepted: 9 November 2016 / Published online: 1 December 2016
© Springer-Verlag Berlin Heidelberg 2016

Abstract In the geologic record, the quartz *c*-axis patterns are widely adopted in the investigation of crystallographic preferred orientations (CPO) of naturally deformed rocks. To this aim, in the present work, four different methods for measuring quartz *c*-axis orientations in naturally sheared rocks were applied and compared: the classical universal stage technique, the computer-integrated polarization microscopy method (CIP), the time-of-flight (TOF) neutron diffraction analysis, and the electron backscatter diffraction (EBSD). Microstructural analysis and CPO patterns of quartz, together with the ones obtained for feldspars and micas in mylonitic granitoid rocks, have been then considered to solve structural and geological questions related to the Montalto crustal scale shear zone (Calabria, southern Italy). Results obtained by applying the different techniques are discussed, and the advantages

as well as limitations of each method are highlighted. Importantly, our findings suggest that patterns obtained by means of different techniques are quite similar. In particular, for such mylonites, a subsimple shear (40% simple shear vs 60% pure shear) by shape analysis of porphyroclasts was inferred. A general tendency of an asymmetric *c*-maximum near to the *Z* direction (normal to foliation) suggesting dominant basal slip, consistent with fabric patterns related to dynamically recrystallization under greenschist facies, is recognized. Rhombohedral slip was likely active as documented by pole figures of positive and negative rhombs (TOF), which reveal also potential mechanical Dauphiné twinning. Results showed that the most complete CPO characterization on deformed rocks is given by the TOF (from which also other quartz crystallographic axes can be obtained as well as various mineral phases may be investigated). However, this use is restricted by the fact that (a) there are very few TOF facilities around the world and (b) there is loss of any domainal reference, since TOF is a bulk type analysis. EBSD is a widely used technique,

Electronic supplementary material The online version of this article (doi:10.1007/s00531-016-1424-y) contains supplementary material, which is available to authorized users.

✉ Eugenio Fazio
efazio@unict.it

Rosalda Punturo
punturo@unict.it

Rosolino Cirrincione
r.cirrincione@unict.it

Hartmut Kern
kern@min.uni-kiel.de

Antonino Pezzino
pezzino@unict.it

Hans-Rudolf Wenk
wenk@berkeley.edu

Shalini Goswami
shalinigoswami92@gmail.com

Manish A. Mamtani
mamtani@gg.iitkgp.ernet.in

- ¹ Department of Biological, Geological and Environmental Sciences, Catania University, Corso Italia 57, 95129 Catania, Italy
- ² Institute of Geosciences, CAU University of Kiel, Olshausenstr. 40, 24098 Kiel, Germany
- ³ Department of Earth and Planetary Science, University of California, Berkeley, CA 94720, USA
- ⁴ Department of Geology and Geophysics, Indian Institute of Technology, Kharagpur, West Bengal 721302, India

which allows an excellent microstructural control of the user covering a good amount of investigated grains. CIP and US are not expensive techniques with respect the other kind of investigations and even if they might be considered obsolete and/or time-consuming, they have the advantage to provide a fine and grain by grain “first round” inspection on the investigated rock fabric.

Keywords Rock fabric · Crystallographic preferred orientation (CPO) · Quartz · Mylonite · Time-of-flight neutron diffraction (TOF) · Electron backscatter diffraction (EBSD)

Introduction

Quartz *c*-axis orientation patterns are employed fundamentally to understand the shear sense of mylonitic rocks. Such stereographic plots have been widely adopted in the geological literature in order to evaluate various tectonic processes, from the restoration of crustal blocks geometrical position up to the reconstruction of tectonic transport direction within a collisional belt (e.g., Sander 1930, 1950; Anderson 1945; Schmid and Casey 1986; Lister and Hobbs 1980). Several authors (e.g., Mainprice et al. 1986; Law et al. 1990; Okudaira et al. 1995; Takeshita et al. 1999; Leissa et al. 2000; Stipp et al. 2002; de Araujo et al. 2003; Kilian et al. 2011; Law 2014; Punturo et al. 2014; Keppler et al. 2015; Faghih and Soleimani 2015) have implemented this approach to solve questions regarding the estimation of strain, the degree of non-coaxiality of a shear zone, and the thermal deformational range. Some of these issues can be addressed qualitatively from kinematic/shear sense indicators (Mukherjee 2011, 2012). Therefore, quartz *c*-axis study can be used to be doubly sure about shear zone kinematics.

Moreover, a series of laboratory experiments have been done on analog materials (Ree 1994) as well as on syn-kinematic microscopy on CPO of experimentally deformed quartz- and feldspar-rich aggregates (Dell’Angelo and Tullis 1989; Heilbronner and Tullis 2006) to monitor fabric evolution at controlled pressure, temperature and stress conditions and to compare them with quartz crystallographic preferred orientation (CPO) patterns in naturally sheared quartz-feldspar bearing rocks.

After the first published fabric diagram obtained with the universal stage (Schmidt 1925), several techniques have been applied to measure CPO of quartz, including a photometric method (e.g., Price 1973), a modified optical microscope (e.g., Wilson et al. 2007), a computer controlled rotating polarizer stage for the petrographic microscope (e.g., Fueten 1997; Goodchild and Fueten 1998), X-ray pole figure measurements (e.g., Baker et al. 1969),

neutron diffraction (e.g., Frischbutter et al. 2000), synchrotron X-ray diffraction (e.g., Wenk et al. 2006) and electron backscatter diffraction (e.g., Prior et al. 1999, 2009). This work compares results from four techniques, from the most obsolete to the modern and advanced ones, and we apply them to a suite of mylonitic samples from the Montalto shear zone (MSZ, Calabria, Italy). They consist of: (1) orientation measurements of quartz *c*-axis with a classical petrographic microscope equipped with a universal stage, US (Phillips 1971 and references therein); (2) a semi-automated technique based on the image analysis of quartz domains in thin section, the CIP method (computer-integrated polarization microscopy) introduced by Panozzo-Heilbronner and Pauli (1993) and modified by Heilbronner (2000b); (3) time-of-flight neutron diffraction (Wenk et al. 2003); (4) electron backscatter diffraction, EBSD (Prior et al. 1999).

We consider whether quartz CPOs obtained by means of US, CIP, TOF and EBSD are comparable by taking into account that each technique gives a piece of information related to the volume/area under investigation. Indeed, the same thin sections were investigated by US and CIP techniques, whereas rock cylinders from the same samples have been used for the neutron diffraction analysis and additional ultra-polished thin sections were cut from the same specimens parallel to the stretching lineation and perpendicular to foliation for EBSD analyses. Note that thin sections analyzed with EBSD derive by serial sectioning of the same specimen investigated by CIP, US, providing equivalent quartz domains. In order to make various datasets consistent with each other, the crystallographic quartz *c*-axis orientations determined by means of US have been stored in a database (plunge and azimuth measurement of *c*-axis for each quartz grain with respect a reference direction the strike of mylonitic foliation) and rotated using the Stereonet software (Duyster 1996). This allowed us to represent on pole figures quartz *c*-axis orientations acquired by US consistently with respect to the other techniques.

We will discuss advantages and disadvantages of each method, also illustrating the potential usefulness of results for structural geology.

Geology and samples

Investigated sheared rocks belong to the Aspromonte unit (AU), a tectonic nappe of medium to high grade Variscan tectono-metamorphic unit (Fiannacca et al. 2013) composed essentially of gneisses, schists, and granitoids, which participated in the Alpine orogeny (Pezzino et al. 2008; Ortolano et al. 2005). These mylonites occur along the Montalto crustal scale shear zone (MSZ) cropping out in the Aspromonte Massif (Fig. 1), southern Calabria, Italy

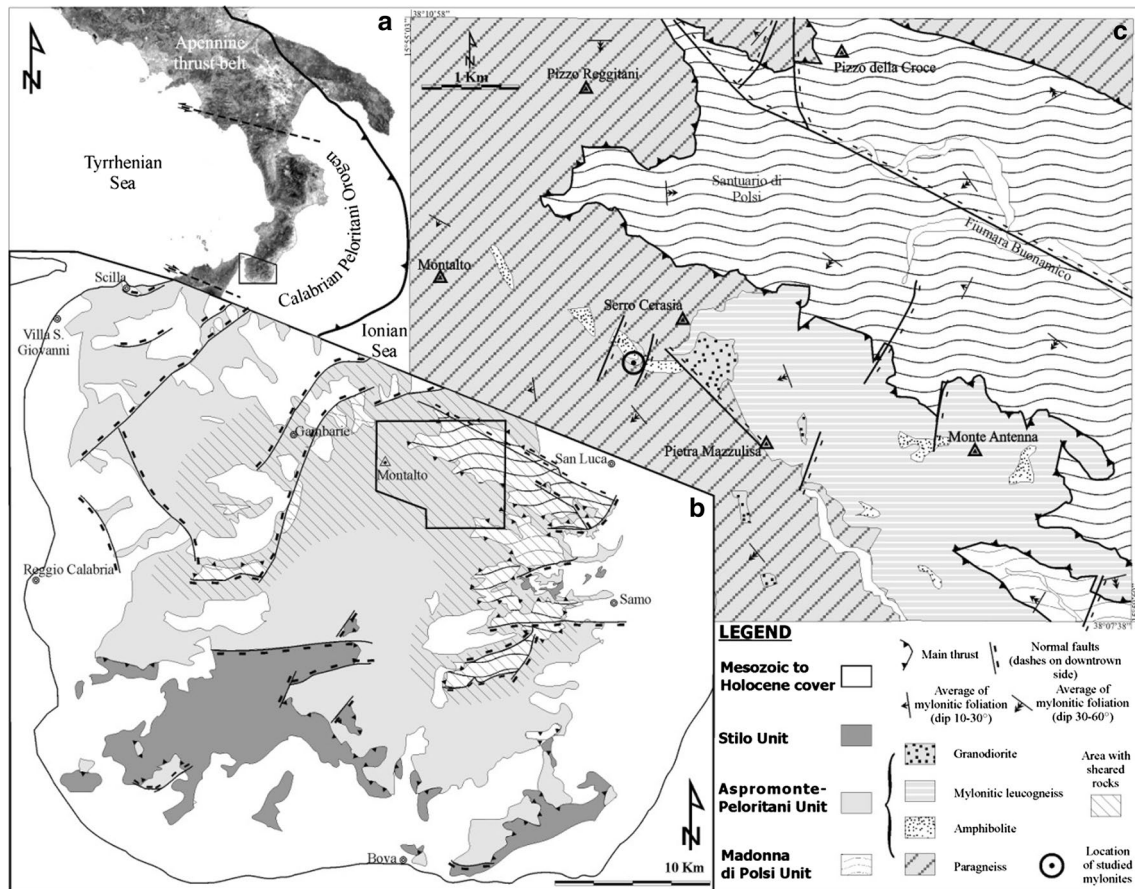


Fig. 1 Study area location and geological sketch map of Aspromonte Massif (southern Calabria): **a** southern Italy region; **b** Aspromonte Massif simplified geological map; **c** study area and sample location

(Pezzino et al. 1990; Fazio et al. 2008, 2009, 2010, 2015; Cirrincione et al. 2012, 2015).

The rocks of the AU are the result of a relic Variscan metamorphic LP–HT cycle (Graessner et al. 2000; Fianacca et al. 2012, 2013), in which mineral assemblages were overprinted by a later HP–LT Alpine mylonitic shear. The low $\Delta P/\Delta T$ metamorphism depicts a first stage of prograde evolution (~ 0.56 GPa at ~ 570 °C) evolving toward peak conditions (0.63–0.93 GPa at 650–710 °C) linked to crustal thickening, followed by a crustal thinning documented by the retrograde path (0.25 GPa at ~ 540 °C, after Cirrincione et al. 2008).

The late Alpine mylonitic overprint (Pezzino et al. 2008 and references therein) was ascribed to the late Oligocene rapid uplift/exhumation along a deep-seated compressional shear zone (Cirrincione et al. 2012). Late Alpine mylonitization and metamorphism ~ 25 Ma (Thomson 1994) involved a quasi-adiabatic retrograde decompression path (~ 0.75 GPa at 570–600 °C), fitting a fast exhumation mechanism, and evolved to a cooling trajectory ranging from ~ 0.38 GPa at 450–520 °C (Cirrincione et al. 2008, 2012).

The leucogneiss outcrop (Fig. 2; UTM coordinates: 4223090N, 582412E), affected by a later brittle deformation history, is characterized by a well-preserved strain gradient, which in the whole Aspromonte Massif area essentially increase toward NNE over a distance of about 8 km. A sequence of increasingly deformed specimens derived from an igneous protolith was already investigated to determine rock rheology within a narrow shear zone (Cirrincione et al. 2009, 2010, 2013), and the same specimens were selected for this study. The grain-size variability, into the mylonitic shear zone, is due to inhomogeneous distribution of strain during progressive deformation as described by Cirrincione et al. (2010). Four highly foliated rock samples (M13, M8, M3 and M4), showing usually a clear mylonitic foliation (averagely oriented $N150^\circ/20^\circ/SW$ as azimuth/dip/dip direction) and a stretching lineation gently dipping alternatively NNE or SSW (indicating a top-to-the-NE sense of shear in present-day geographic coordinates; Fig. 2c), were collected along a transect characterized by a uniformly increasing strain gradient (Figs. 2b, 3). This shear is related to the D_3 deformational phase (Pezzino et al. 2008). Mylonites were taken at varying distance from

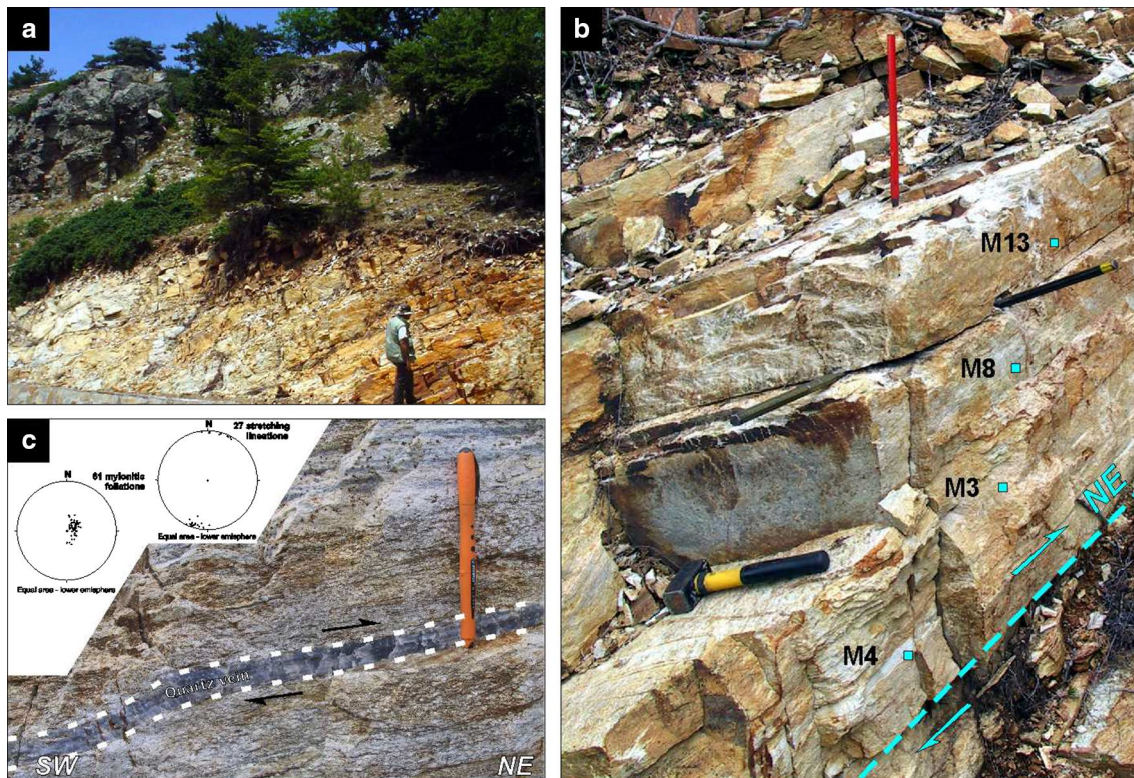


Fig. 2 **a** Outcrop view; **b** sampling site of mylonitic rocks (*M13*, *M8*, *M3*, and *M4* specimens). Hammer handle is about 80 cm long; **c** Mesoscopic view of a quartz-rich level within the leucogneisses, in the

upper left inset stereoplots showing poles to foliation and stretching lineation are illustrated

a mesoscopic shear zone in the field (visible in the bottom part of Fig. 2b) by maintaining a constant sampling interval of about 20–25 cm. The strain gradient, which is readily manifested at outcrop scale (Fig. 2b, c), was inferred by grain shape analysis of selected quartz microdomains from the various specimens (Cirrincone et al. 2010). This is also confirmed by analysis of rigid porphyroclasts carried out for this study (section “[Mineralogy and microstructures](#)”).

Chemical and modal rock composition

Mineral chemistry and bulk rock analyses of the sheared leucogneiss samples have been performed by X-ray fluorescence (XRF) along with the electron microprobe analysis (see “[Appendix 1](#)” for instrumental conditions). Both data sets were used to calculate the modal composition of the studied rocks (Table 1). The calculation of the mineral modes is performed following the generalized petrological mixing model of Le Maitre (1979) using the computer program PetMix (<http://www.geology.net/programs/petmix410.xls>), which is based on a least square fit. In contrast to point-counting and EBSD measurements, this approach includes large rock volumes, thus providing

statistically more reliable results. Importantly, in strongly foliated rocks with marked shape preferred orientation (SPO) of major minerals, accurate determination of volume percentages by point counting or EBSD is difficult, even if three perpendicular oriented thin sections are used. This particularly holds for rocks exhibiting pronounced mm-size heterogeneities. Quartz (31–38 vol%) and plagioclase (35–60 vol%) are the dominant mineral phases in all four samples (Table 1). K-feldspar is also an important constituent of samples *M13*, *M3* and *M8* mylonites (about 17, 8, and 7, respectively). However, most obvious are the marked differences in the content of phyllosilicate minerals (biotite, muscovite)—in samples *M13*, *M8*, *M3* phyllosilicates contribute about 6–19 vol%, whereas in sample *M4* their content is minimal (about 1 vol%). The phyllosilicate content exerts a strong influence on the strain partitioning and bulk rock rheology as well as the spatial distribution coupled with the interconnectivity of such minerals could have an effect on quartz CPO (e.g., Renjith and Mamtani 2014; Hunter et al. 2016). To avoid such consequences, we selected quartz microdomains away from large flakes of mica. As already demonstrated for the selected samples, the aligned mica enhances anisotropy (Cirrincone et al. 2010).

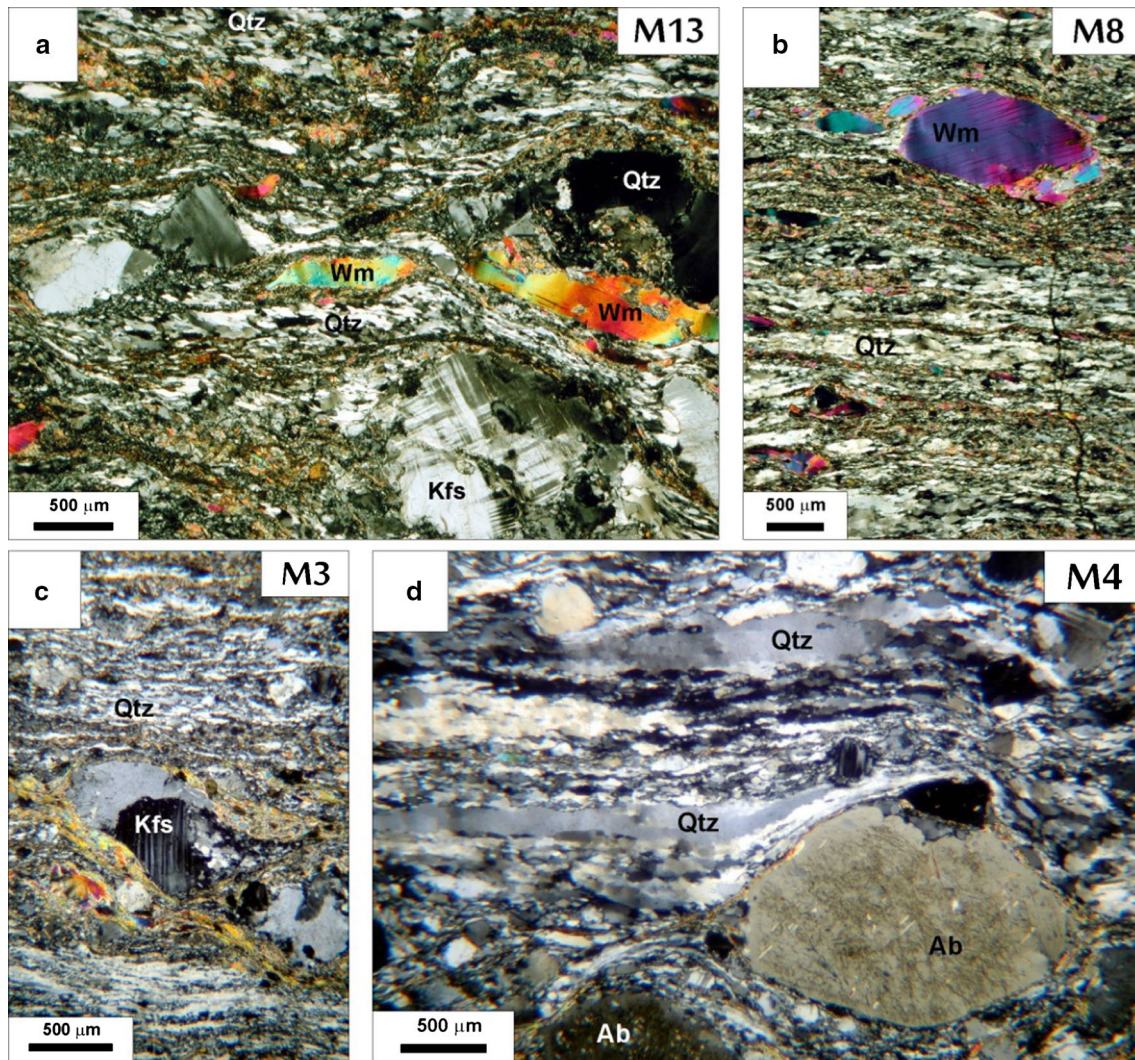


Fig. 3 Microphotographs of various investigated mylonites (W_m white mica, Qtz quartz, Kfs alkali feldspar, Ab albite): **a** sample M13; **b** sample M8; **c** sample M3; **d** sample M4

Table 1 Mineral abundances (vol%): (a) calculated with PetMix spreadsheet, based on whole-rock and mineral compositions; (b) determined by MAUD software

Sample	M13		M8		M3		M4	
	a	b	a	b	a	b	a	b
Quartz	31.5	35.7	33.6	24.2	34.8	30.8	37.9	31.9
Plagioclase	36.3	35.4	36.9	19.2	35.3	31.8	59.3	66.8
K-Feldspar	17.7	16.0	6.8	47.5	8.1	27.9	–	–
Muscovite	6.4	9.5	15.7	9.1	19.4	8.0	1.2	1.3
Biotite	4.3	3.4	–	–	–	1.5	0.5	–
Epidote	3.8	–	7.1	–	2.4	–	1.1	–

Different sample volumes were used for the analyses

Mineralogy and microstructures

The collected samples of leucocratic gneisses are mostly composed of quartz, plagioclase, alkali feldspar and white

mica (Fig. 3a–d), with subordinate garnet, biotite, epidote, chlorite and tourmaline. The occurrence of tourmaline testifies significant localized fluid circulation with high boron content, typical of crustal scale shear zones (Sengupta et al.

2005). S–C and S–C' fabrics, and mineral fish (Passchier and Trouw 2006; Mukherjee 2013a) are widespread in all of the samples (Fig. 3). Ribbon-like quartz is very common too. Different recrystallization mechanisms of quartz such as rare bulging and grain boundary migration, and dominant subgrain are typical of greenschist up to lower amphibolite facies metamorphism. The progressive development of a mylonitic fabric is documented by the decreasing grain size of the pre-kinematic porphyroclasts (usually feldspars) from sample M13–M4 toward NNE over a distance of about 1 m and accompanied by progressive syn-kinematic growth of small grains of white mica, which is texturally in equilibrium with subgrain crystallization of quartz and subordinate chlorite.

To estimate the mean kinematic vorticity number (W_m) in Fig. 4) and semiquantitatively define the strain gradient within the suite considered here, the rigid grain net method (RGN, detail in Jessup et al. 2007) was performed on the entire area of each thin section cut from the four selected samples (Fig. 4). Grain boundary maps of rigid clasts constituting porphyroclasts (usually K-feldspar) were manually traced on high-resolution scan images (12,000 dpi) of thin sections acquired both with parallel and crossed polars.

Results match well with the shape analysis of quartz grains (after Cirrincione et al. 2010), showing an increasing aspect ratio ($R = \text{long axis/short axis}$; see “Appendix 3”) from sample M13 ($R = 1.488$), through sample M8 ($R = 1.528$), to sample M3 ($R = 1.842$) except for the M4 sample, which shows the lowest R value ($R = 1.407$). Note that the average grain size as well as the mean shape factor (B^* , after Jessup et al. 2007) of porphyroclasts in this last sample is the lowest.

The least strained sample M13 is characterized by an S–C fabric (Fig. 5a) defined by alignment of mica and quartz-rich layers enveloping K-feldspar porphyroclasts (Fig. 3a). Ribbon-like quartz structures are well developed where larger relict grains with diffuse undulatory extinction are surrounded by smaller new ones, forming an incipient oblique foliation parallel to the S foliation.

Sample M8 (Fig. 5b) is characterized by S–C–C' fabric and rounded porphyroclasts essentially of white mica fishes (Fig. 3b) and lozenge-shaped feldspars, which are characterized by recrystallized quartz and muscovite tails. Large relict quartz grains with undulatory extinction are almost entirely replaced by the syn-tectonically recrystallized smaller grains, which sometimes give rise to an oblique foliation. Grain boundary migration recrystallization of quartz and incipient subgrain rotation recrystallization were also observed. They probably reflect strain accommodation by dislocation creep mechanisms (Cirrincione et al. 2009).

Sample M3 (Fig. 5c) displays a pervasive S–C fabric in the porphyroclastic domains; ribbon-like quartz layers are less well-developed and only the C plane is observed.

K-feldspar porphyroclasts (Fig. 3c) commonly have plagioclase inclusions. Micas on this sample are less than in sample M8, while syn-tectonic recrystallization of a fine mixture of white mica, quartz and epidote as well as myrmekite colonies are more evident. A top to NE ductile shear sense, matching our field observations and recognized by Ortolano et al. (2005) in the same area, was decoded from mineral fish and S–C fabric. Quartz grains are preferentially elongated along C surfaces and form ribbon-like domains, suggesting that a pure shear component worked (Mukherjee 2013b). This also come out from W_m study (Fig. 4) with a minor axis (b) angle of rigid grains on average at 93.74° with respect to the main foliation (primary shear C plane).

The most strained sample (M4, Fig. 5d) has a dominant porphyroclastic microstructure with S–C–C' intersecting foliations. Quartz ribbons either entirely mantle porphyroclasts (Fig. 3d), or constitute independent regularly spaced (~1 cm) levels of recrystallized quartz. Note that this specimen is composed of two parts with distinct grain size and mineral phases consisting of alternating layers parallel to the main mylonitic foliation, they are: (1) a minor portion (~30 vol%) characterized by very narrow shear zones (white arrows in Fig. 3d) where quartz representing the dominant constituent occurs both as fine grained aggregates or ribbons; and (2) a major portion (~70 vol%) usually made up of larger crystals (compared with the shear zones), mainly consisting of rounded feldspar porphyroclasts, flakes of mica and quartz.

Quartz CPO measurement

Quartz c -axis orientations were measured on thin sections cut perpendicular to the mylonitic foliation and parallel to the stretching lineation (XZ planes) using either: (1) universal stage equipped microscopy (US), extended to the entire thin section(s) producing good statistical results and, (2) computer-integrated polarization microscopy (CIP), applied to specific microdomains giving results that are not statistically relevant to the bulk sample but do provide domainal control on CPO development. On cylindrical samples, time-of-flight (TOF) neutron diffraction investigated the crystallographic orientations of various minerals (quartz, white mica, and plagioclase), producing the best statistical results but with a loss of information about CPO in microdomains. Neutron pole figures were rotated into the same plane in which thin sections were studied (i.e., XZ plane). EBSD analyses were carried out on thin section from the same specimens that were cut parallel to the mineral lineation and perpendicular to mylonitic foliation. Figure 6 compares quartz c -axis fabrics measured by four methods for samples M13, M3, M8, and M4 is depicted. In Fig. 6a, b, the universal stage (US) and the computer-integrated polarization

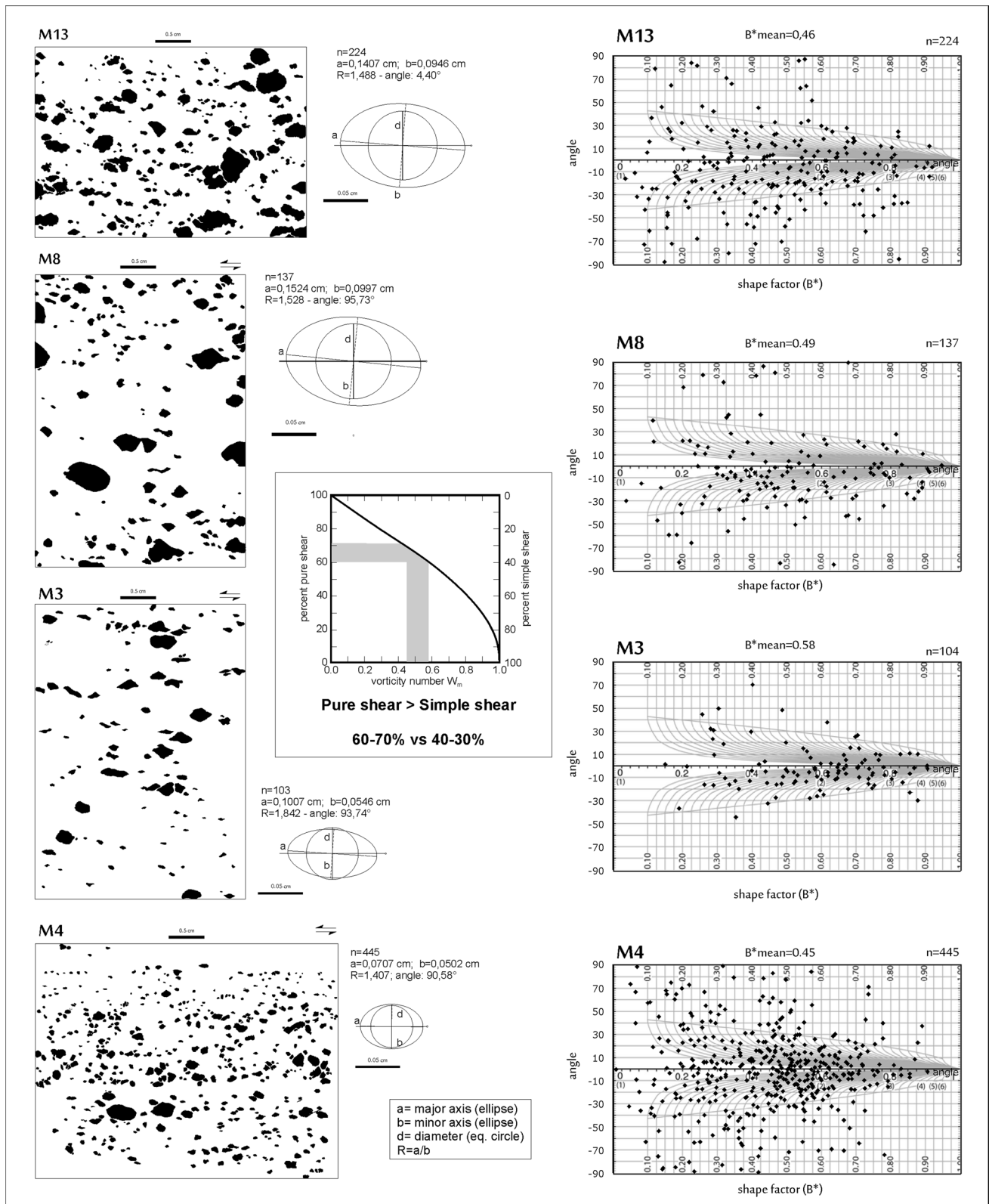


Fig. 4 Rigid grain net (RGN) analysis of porphyroclasts of four mylonites (*M13*, *M8*, *M3*, and *M4*). On the *left*, manually digitized objects together with mean shape grain information are shown (*a* ellipse major axis, *b* ellipse minor axis, *d* equivalent radius; see “Appendix 3”). On the *right*, the angle of major axis particle versus

the shape factor B^* plot for each specimen is shown. In the central inset, the gray area on the mean vorticity number (W_m) versus pure/simple shear percent graph represents the B^* interval calculated for the four specimens

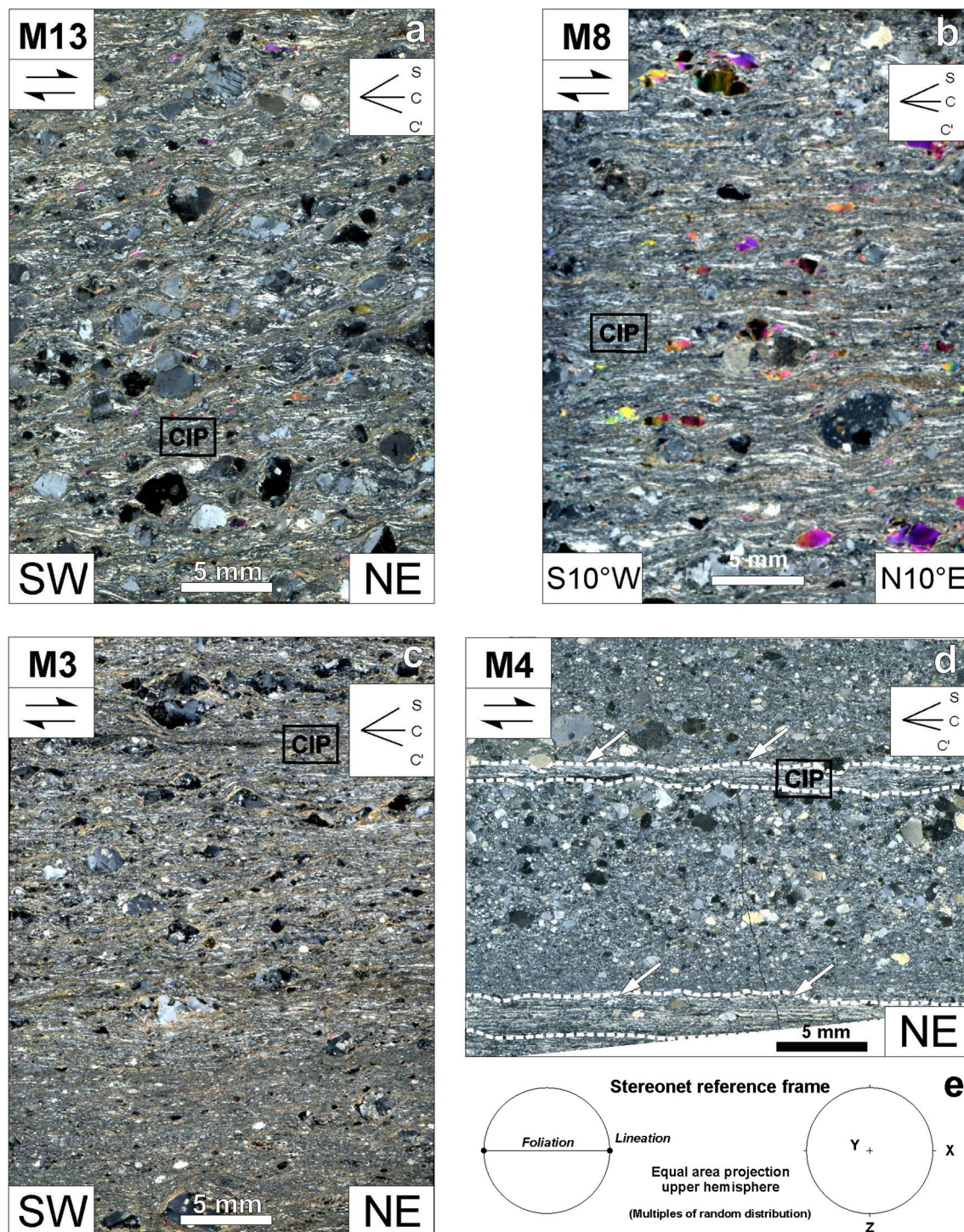


Fig. 5 Microphotographs of entire thin sections acquired by a flat bed scanner (Epson Perfection 3490 Photo) at a resolution of 1200 dpi (crossed polarizers): **a** M13; **b** M8; **c** M3; **d** M4; white arrows indicate the occurrence of millimeter thick narrow shear zone where

microscopy (CIP) are shown, respectively. The *c*-axis pole figures with gray levels correspond to linear increments of 1 times uniform (modified after Cirrincione et al. 2010). In

CIP measurements were carried out (square); S–C–C' fabric orientations are also illustrated in the top-right inset; **e** stereonet reference frame where X and Z designate direction of lineation and pole to the foliation, respectively

Fig. 6c, d the results of time-of-flight (TOF) technique and the EBSD results are shown, respectively. Figure 6e shows the stereonet reference frame with XYZ directions and a 3D

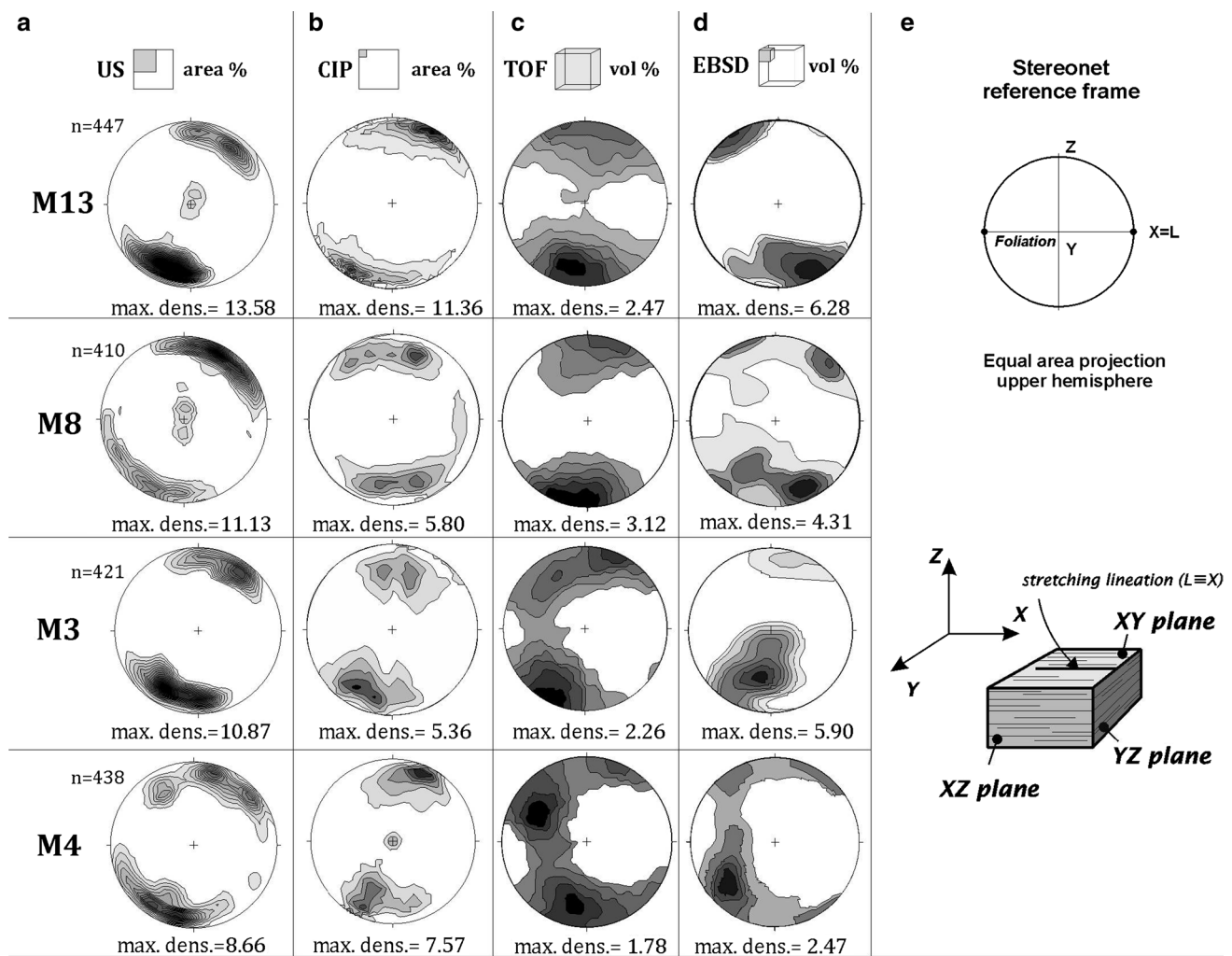


Fig. 6 Comparison of quartz *c*-axis fabrics measured by four methods for samples *M13*, *M3*, *M8*, and *M4*: **a** universal stage (US); **b** computer-integrated polarization microscopy (CIP). The *c*-axis pole figures with gray levels correspond to linear increments of 1 times

uniform (modified after Cirrincione et al. 2010); **c** time-of-flight (TOF); **d** EBSD results; **e** stereonet reference frame with XYZ directions and a 3D sketch showing the XZ plane which has been considered for all of the techniques

sketch showing the XZ plane which has been considered for all of the techniques.

Universal stage (US)

Manual measurements of quartz *c*-axis were performed with a Carl Zeiss Microscope equipped with a classical 3-axis universal stage (Carl Zeiss, model “Pol 460110 Z-Prüf”) and hemispherical lenses with refractive index $n = 1.555$. At least 400 measurements of azimuth/inclination of quartz *c*-axes have been made from each specimen. Density plots (Fig. 6a) were made using the software package Stereonet (v. 2.46) with a grid resolution of 15° on an equal area stereonet (upper hemisphere), counting the number of orientations within a small circle representing 1% of the whole area. Contour lines (integers) are plotted

as multiples of a random distribution. Figure 6a shows stereoplots.

Computer-integrated polarization (CIP) microscopy

On the same thin sections, we measured *c*-axis orientations adopting the CIP method (see “Appendix 2”; Panozzo-Heilbronner and Pauli (1993); Heilbronner 2000b). As fully described by van Daalen et al. (1999), the CIP analysis is based on the visible light microscope and goes back to the ‘Achsenverteilungsanalyse’ (analysis of distribution of axes), which was introduced by Sander (1930) for Universal stage measurements and to the photometric analysis by Price (1973). The CIP method uses the dependence of colors and color changes of uniaxial minerals on the crystallographic orientation in order to derive azimuth

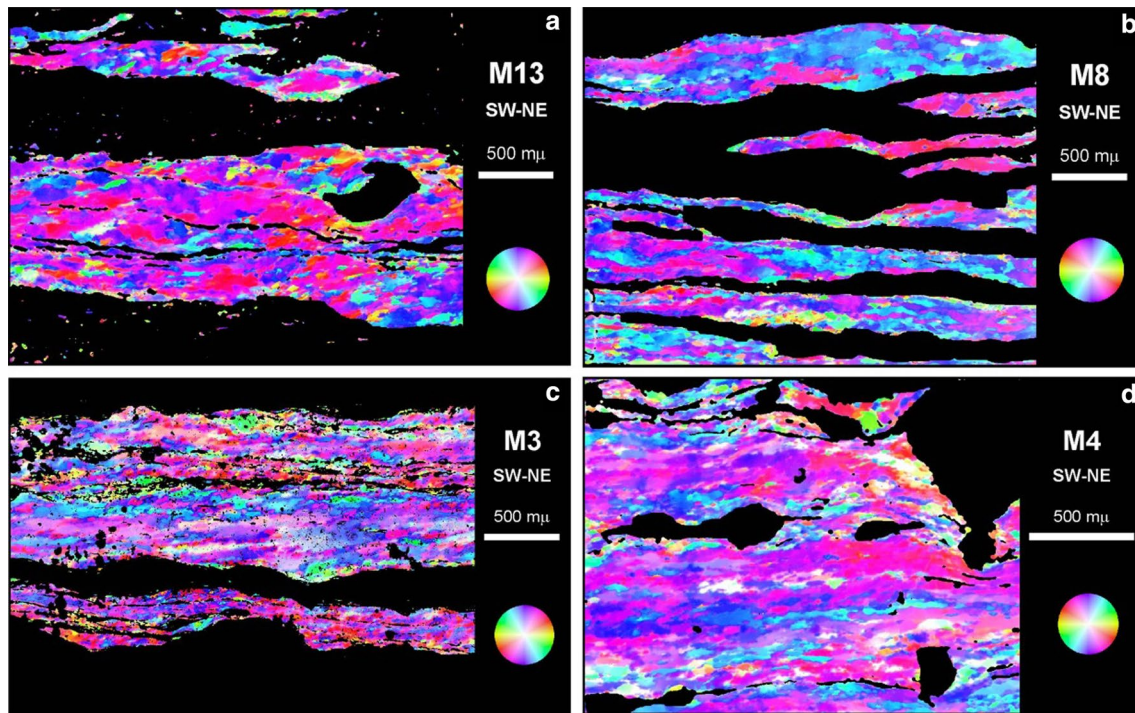


Fig. 7 Quartz *c*-axis orientation images (COIs) inferred by means of CIP (computer integration polarization microscopy) on the same areal domains shown in Fig. 3: **a** M13; **b** M8; **c** M3; **d** M4

and inclination of *c*-axes at each pixel of the image. This yields high-resolution orientation images where microstructural features and *c*-axes orientations superpose (Pauli et al. 1996). Therefore, the microfabric can be presented as *c*-axis orientation images (COIs, Fig. 7a–d) in which the CPO can be directly inferred from the actual colors of grains and domains (e.g., Peternell et al. 2011). Minerals (e.g., feldspar) other than quartz are optically recognized within the acquired domain. To avoid misleading results about quartz *c*-axis orientations, such phases are discarded by software applying automatically or manually shaped masks. Quartz *c*-axis patterns are shown in Fig. 6b (modified after Cirrincione et al. 2010). The reference coordinate system is the same as for universal stage (US) measurements. For all sites, the foliation (*XY* plane) is horizontal and conventional maxima are expressed in multiples of a uniform distribution. The true pixel size for all investigated domains is 2.44 micron since we used a 2× objective.

TOF neutron diffraction method

Cylindrical samples, 1.2 cm in diameter and 1.5 cm long with the cylinder axis parallel to the lineation *X*, were measured on the HIPPO TOF neutron diffractometer at the Los Alamos Neutron Science Center (LANSCE). Neutron diffraction is the optimal method for studying textures of relatively coarse-grained polyphase materials due to low

attenuation allowing investigation of large samples. With TOF measurements of polychromatic neutrons, every detector records a continuous spectrum that includes many diffraction peaks. The HIPPO diffractometer was designed for texture measurements, with 30 detectors arranged in three rings that cover a large part of pole figure space (Wenk et al. 2003; Matthies et al. 2005). The sample was rotated about the cylinder axis into six positions to increase the pole figure coverage, resulting in 180 spectra. Each measurement takes 10–20 min, thus the total time for one sample is 1–2 h. These diffraction spectra were then analyzed with the Rietveld method implemented in the software MAUD (Lutterotti et al. 1997; Wenk et al. 2010, 2012) which provides information about volume fractions of phases (Table 1) and their orientation distributions from which pole figures (Figs. 8, 9, 10) were calculated. Strong CPOs are observed for quartz and mica. Figure 8 gives pole figures for quartz: *c*-axes, *a*-axes (11–20), positive rhombs (10–11) and negative rhombs (01–11). The *c*-axis pole figures are also displayed in Fig. 6c and compared with U-stage and CIP pole figures. TOF *c*-axis pole figures for M13, M8 and M3 show an asymmetric concentration at high angles to the foliation (*Z*). The *c*-axis distribution for M4 is an asymmetric girdle. Significant is a concentration of positive rhombs (10–11) perpendicular to the foliation and a minimum for negative rhombs (01–11). Figure 9 displays (001) pole figures of muscovite. Phyllosilicates in M13, M8 and M3 show a

Fig. 8 Pole figures of quartz obtained with TOF neutron diffraction. Equal area projection, linear contour scale (*m.r.d.* multiples of random distribution). Lineation direction (*X*) is EW, foliation normal (*Z*) NS, intermediate direction (*Y*) at center

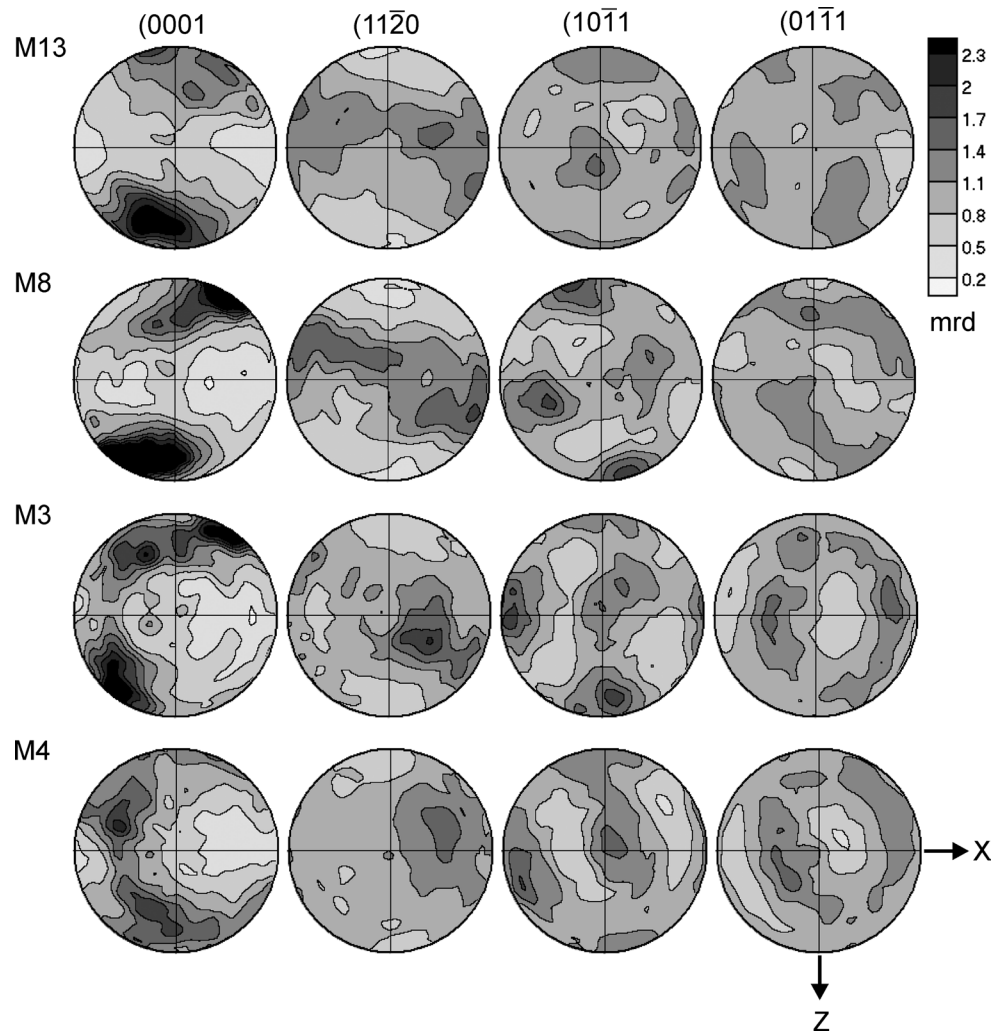
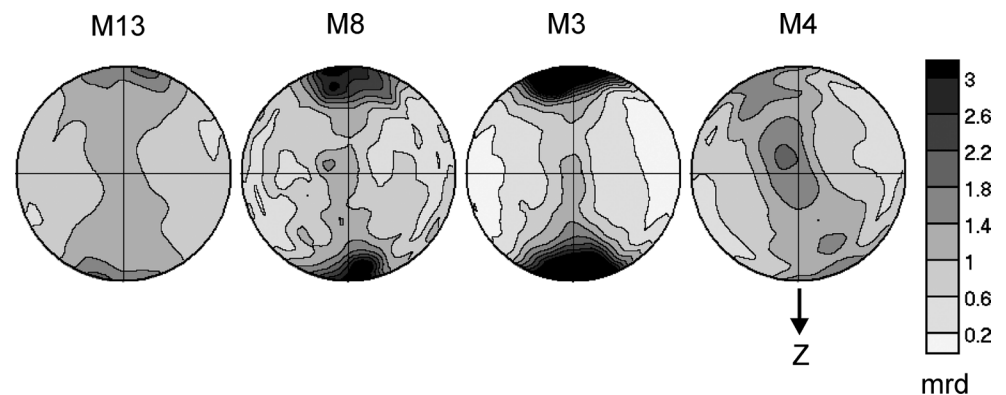


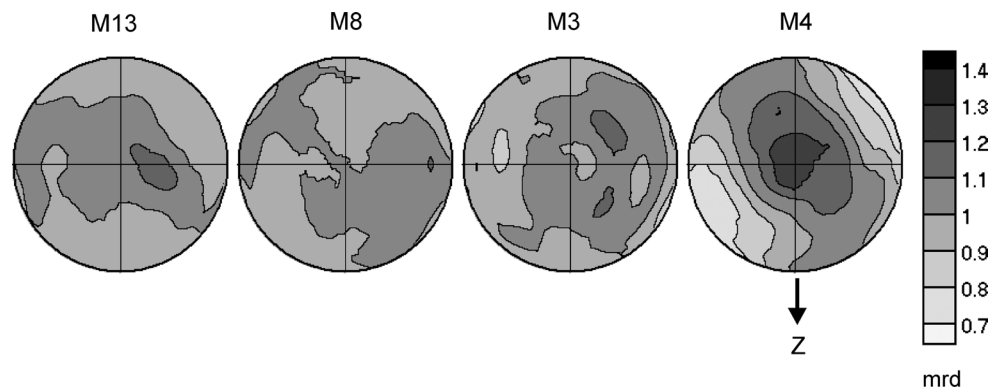
Fig. 9 (001) Pole figures of white mica obtained with TOF neutron diffraction. Equal area projection, linear contour scale (*m.r.d.* multiples of random distribution). Lineation direction (*X*) is EW, foliation normal (*Z*) NS



regular textures with a (001) maximum more or less perpendicular to the foliation C. The texture is strongest for M3. Note that the (001) maximum of quartz in sample M3 is distinctly asymmetric to the foliation, contrary to muscovite

(cf. Figs. 6, 9). For sample M4 the texture is much weaker, with an asymmetric girdle. Textures of plagioclase are basically random, becoming slightly stronger in sample M4 but this may be an artifact (Fig. 10).

Fig. 10 (100) Pole figures of plagioclase obtained with TOF neutron diffraction. Equal area projection, linear contour scale (*m.r.d.* multiples of random distribution). Lineation direction (*X*) is EW, foliation normal (*Z*) NS, intermediate direction (*Y*) at center. All samples display essentially a random orientation distribution



Electron backscatter diffraction (EBSD) analysis

EBSD allows the crystallographic nature of a small volume of bulk crystalline samples to be examined in the scanning electron microscope (SEM). The technique was originally developed in the 1980s, and over recent years there has been rapid development to produce a powerful and sophisticated experimental tool for material characterization (Wilkinson 1999). Dingley (2004) reviewed the development of the EBSD technique. EBSD data can also be used to analyze strain (e.g., Wright et al. 2011; Renjith and Mamtani 2015).

Current systems typically capture and solve EBSD patterns to obtain crystal orientations automatically at rates of one measurement per second (or faster) from regions a few hundred nanometers in size (Wilkinson 1999). The analysis not only provides orientations of all the crystallographic axes that can be used to prepare inverse pole figure maps and pole figures, but also generates voluminous statistical data about size-, shape- and orientation of grains. All this information can be used for kinematic analysis and also for shape preferred orientation (SPO) studies (e.g., Bestmann et al. 2000; Neumann 2000; Jeřábek et al. 2007; Renjith et al. 2016 among others). Importantly, EBSD has been successfully applied to quartz both to decipher grain boundary migration mechanisms (and/or deformation mechanism) as well as to unravel history and dynamics of crustal tectonic processes (e.g., Prior et al. 1999).

In the present study, electron backscatter diffraction analysis (EBSD) was carried out at the Central Research Facility (CRF of IIT, Indian Institute of Technology Kharagpur, India) on thin sections cut parallel to the *XZ* plane of the above four samples. Texture analysis were made using Carl Zeiss Auriga Compact FEG-SEM fitted with Nordlys Max2 EBSD detector (Oxford instruments, UK). Figure 6d shows the results of such investigation for quartz *c*-axis. EBSD patterns were generated at 25 kV accelerating voltage, 1.49×10^{-6} mbar system vacuum, and ~14 mm working distance. Data acquisition and indexing of EBSD patterns were carried out automatically using AZtec software (Oxford instruments, UK). Mapping

of quartz grains (10 μm step size) was done for multiple frames in each sample; the area mapped in samples M3, M4, M8 and M13 was, respectively, $1018 \times 10^5 \mu\text{m}^2$, $663 \times 10^5 \mu\text{m}^2$, $778 \times 10^5 \mu\text{m}^2$ and $520 \times 10^5 \mu\text{m}^2$. Acquired data were processed by using HKL CHANNEL 5 software (Oxford Instruments, UK). A standard noise reduction was performed to remove non-indexed points. Figure 11 shows the pole figures (upper hemisphere, equal area) of $\{0001\}$ i.e., *c*-axis, $\{11\text{-}20\}$ i.e., *a*-axis, $\{10\text{-}10\}$, $\{10\text{-}11\}$, and $\{01\text{-}11\}$ of all quartz grains mapped in the four samples. Figure 12 shows the pole figures of sub-areas of sample M4 selected to highlight the effective contribution of each subdomain to the bulk texture (Fig. 6d). Further results from sub-areas of the same sample are available as supplementary material.

Discussion

Comparison of quartz *c*-axis pole figures obtained by US, CIP, TOF and EBSD

Figure 6 compares quartz *c*-axis pole figures of US, CIP, TOF, and EBSD results for the investigated mylonites. Both optical methods (US and CIP) produce *c*-axes aligned close to the *XZ* plane, while *c*-axes inclined to the thin section plane were rarely measured. In contrast, neutron diffraction and EBSD indicate a high proportion of grains have steeply plunging *c*-axes relative to *XZ* plane. Indeed, it is quite evident how the US patterns, and subordinately the CIP ones, are essentially characterized by broad peripheral maxima in all of the specimens (Fig. 6a, b), whereas TOF and EBSD patterns (Fig. 6c, d) show also a single girdle extending from the peripheral maximum toward the pole figure center (i.e., sample M4). EBSD pole figures (Fig. 6d) compare fairly well with plots obtained with the other techniques, with negligible differences about spatial *c*-axis distribution. TOF results (Fig. 6c) show much weaker textures; this is because these results represent averages values obtained over the bulk volume of the mylonite. As

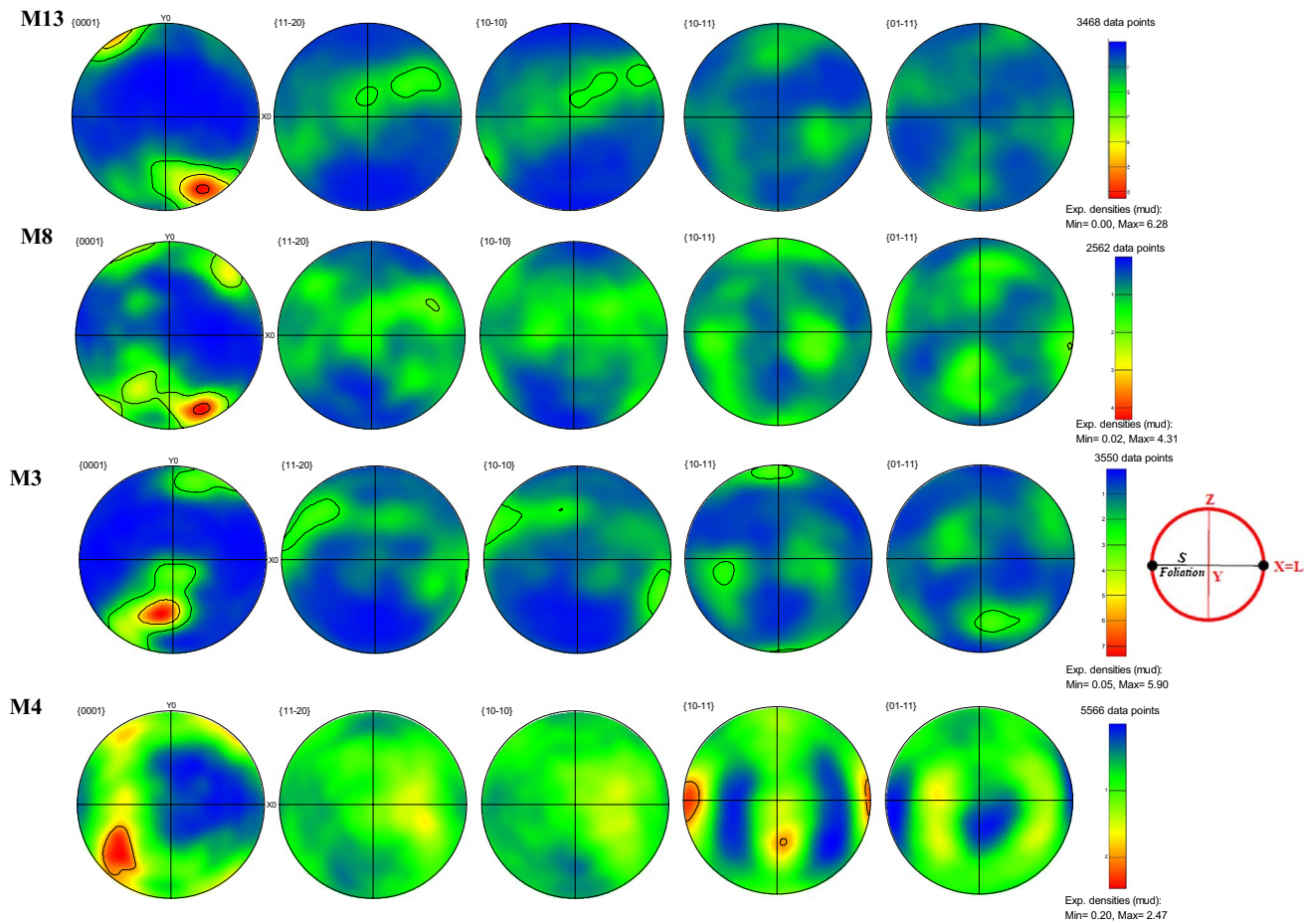


Fig. 11 EBSD pole figures of quartz. Sections are all XZ of strain ellipsoid, where X is horizontal, Z is vertical, and Y is at the center of the pole figures (see reference frame on the right). Diagrams are upper hemisphere, equal area projections (*mud* multiple of uniform distribution)

is qualitatively expressed in Fig. 5, orientation patterns between the pronounced shear bands are much weaker. Patterns obtained with the TOF technique (Fig. 6c, 8) are geometrically consistent with the ones obtained with the US technique (Fig. 6a), CIP (Fig. 6b), and EBSD (Fig. 6d) except for sample M4. For this specimen, two maxima were obtained by TOF (Fig. 6c): one is comparable with the pole figures (cluster near to Z) obtained with the other techniques, whereas the other one occurs close to the X axis, forming a cluster which is rather slight in the US and EBSD plots (Fig. 6a, d) and not observable at all in the CIP plot (Fig. 6b). The EBSD bulk plot of sample M4 reveals a clear maximum that is observable near to the Z direction (Fig. 6d), comparable with TOF, whereas the other *c*-axes are distributed along a girdle. The selected sub-areas of M4 sample (Fig. 12) reveals that the bulk quartz *c*-axis EBSD plot (Fig. 6d) derives from the combination of two different clusters: the first one consists of a double maximum near to the great circle between the Y–X directions (pole figures shown in the upper left corner) and is well documented on the sub-area depicted in the lower left picture (quartz

matrix between two feldspar porphyroclasts in Fig. 12); the second cluster, approximately equidistant from Y, Z, and X directions and describing a very faint single girdle (pole figures shown in the lower right corner), is well developed in the upper right picture (quartz ribbon wrapping a large feldspar porphyroclast in Fig. 12).

On the whole, all of the *c*-axis maxima obtained by each technique (Fig. 6a–d) define an asymmetric trend with respect to lineation and foliation orientations, which fits well the distribution of quartz *c*-axes interpreted to be recrystallized under non-coaxial deformation with a dextral shear sense (Passchier and Trouw 2006). This matches with numerous kinematic indicators observed both at the micro- and meso-scale such as mica-fish, S–C fabrics (Cirrincione et al. 2009, 2010). As far as the girdles recognized in the EBSD pole figure of mylonite M4 and, at a lesser extent of sample M8 (Fig. 6d), they resemble a type I skeleton pattern, which should be compatible with a coaxial deformation (Passchier and Trouw 2006).

Minor discrepancies observed after comparing US and CIP with TOF and EBSD methods are due to: (a) US

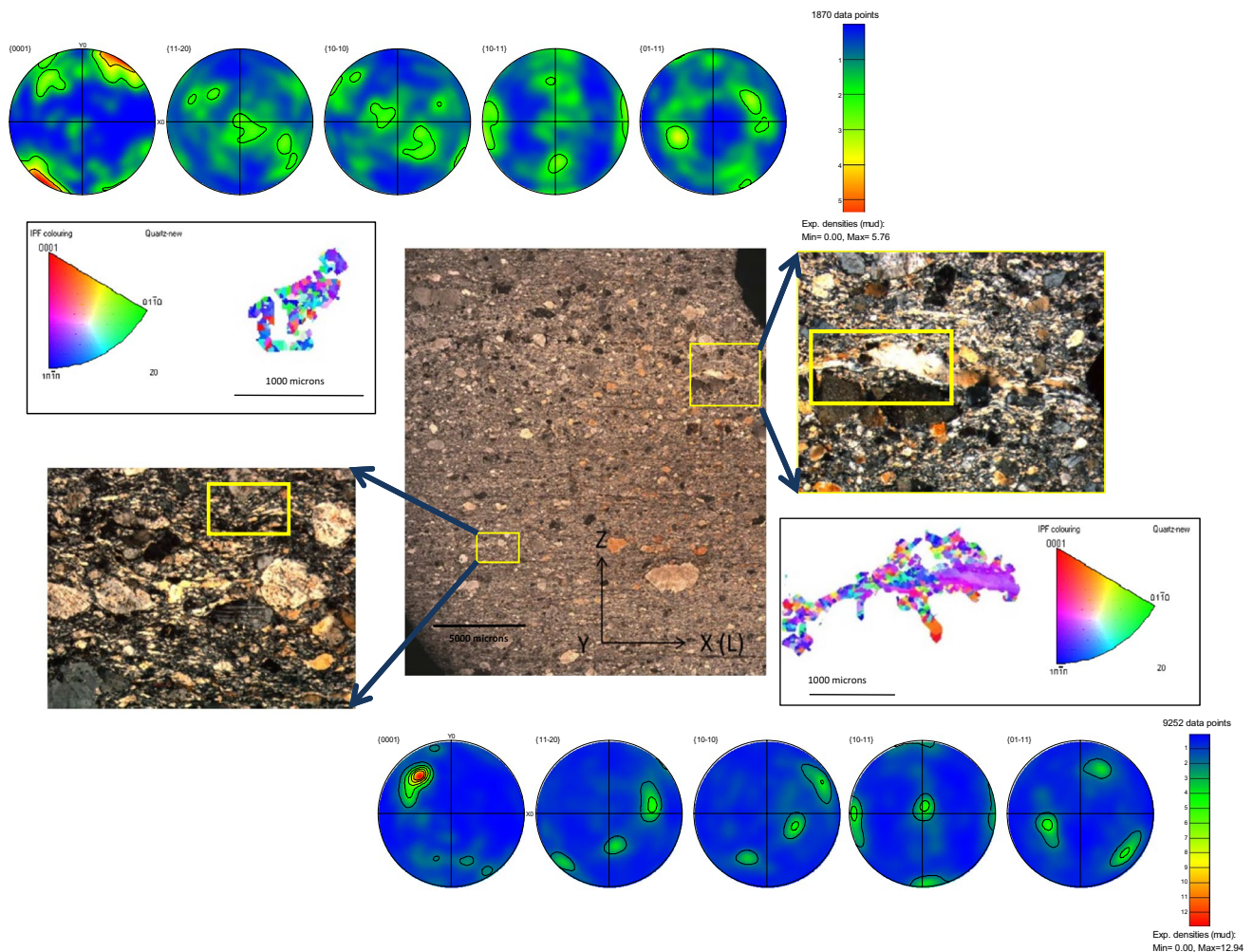


Fig. 12 Thin section scan of sample *M4* (*X*, *Y*, *Z* reference frame is also shown, *L* lineation) with location of two investigated subdomains. EBSD pole figures, CPO color-coded grain boundary maps and inverse pole figures of two selected sub-areas of sample *M4*:

quartz in the matrix (to the *left*, 1870 data points, maximum distribution at 5.76) and ribbon-like quartz (to the *right*, 9252 data points, maximum distribution at 12.94)

usually excludes very small grains; and (b) the CIP method focuses only on millimeter thick narrow shear zones (Figs. 5d, 6b), thus measuring just the special orientation of *c*-axes within the selected quartz domains, which may be not representative of the volume covered by the TOF method as well as of the grain population analyzed by EBSD.

Advantages versus limitations

Table 2 summarizes the important aspects of the four methods. The US has the advantage of direct control on individual grains, even though orientations of grains with size <15 microns can be hardly measured. Moreover, the attainment of CPO optical measurements depends not only on grain size, but also on the shape and orientation of grains relative to the plane of the thin section (e.g., Law et al. 1990).

The thin section is usually 30 microns thick. One should be aware that the US technique (areal investigation) is considered to be time-consuming when data are used to make domainal maps. Nowadays, the manual optical microscope and universal stage method, originally designed by Fedorov in the 1890s for measuring 2 *V* in plagioclase feldspar, is rarely used.

The CIP method, developed by Renée Heilbronner at University of Basel in the early 1990s, is essentially a semi-automated version of the optical microscope and universal stage method (restricted to uniaxial minerals such as quartz) and has some nice features for mapping domainal variations in CPO. Since the CIP method can be considered intrinsically domainal, it is accurate and precise on a restricted region of interest allowing us to establish for each pixel of the image the *c*-axis orientation of grains even showing undulose extinction, which is difficult to obtain

Table 2 Advantages and disadvantages (strong and weak points of each method)

Technique	Measuring time	Availability	Statistical meaning	Advantage w/r to microstructure	Investigate volume	CPO information
US	Several hours/days	Everywhere	Low	Simultaneous information about microstructure	Thin section (small)	Optical axes only (uniaxial and biaxial minerals)
CIP	Hours	Limited	Low	Simultaneous information about microstructure	Thin section (small)	<i>c</i> -axes only (uniaxial minerals)
TOF	Hours	Limited	High	No information	Large volumes (several cm ³)	Full CPO for all phases
EBSD	Hours	Increasing	High	Simultaneous information about microstructure	Small volumes (thin section scale)	Full CPO for all phases

with US, but the investigable area is quite reduced (usually ca. 1 mm²). What is more, the user should collect *c*-axis orientations from various domains to reach a statistical meaningful dataset (e.g., Kilian et al. 2011). In mylonitic rocks, by selecting certain regions of interest (according to grain size or given crystallographic directions), one can also obtain partial pole figures. Besides, the CIP technique, which yields reliable information on selected domains, has the advantage to be relatively fast (Table 2).

TOF, which is a volumetric investigation, is undoubtedly advantageous to represent bulk distributions. Moreover, when quartz-bearing rocks are investigated, an advantage of TOF is that it determines full orientation distributions (Figs. 6c, 8), not just *c*-axes and this is critical for interpreting deformation mechanisms. As mentioned earlier, pole figures of positive and negative rhombs differ (Fig. 8). Neutron diffraction offers some distinct advantages, particularly for large bulk samples with several mineral components, and also provides orientation information for feldspars and micas (Figs. 9, 10).

Finally, the EBSD technique, which is currently one of the most used methods for quartz CPO determination, allows integrated microstructural control and full crystallographic orientation for several minerals within selected domains. EBSD and its dedicated post-processing software available in many laboratories probably represent the most impressive method for achieving domain mapping of CPOs. Indeed, EBSD gives information of: (a) entire thin section—including grains smaller than 20 microns in size; (b) domains of thin section by making subsets (e.g., Fig. 12); and (c) complete crystallographic data (i.e., *c*- as well as *a*-axes in quartz, Fig. 11). It is important to note that although EBSD gives complete crystallographic information, which is similar to TOF neutron diffraction, the area investigated using the latter is far more than that studied using the former. However, SEM's fitted with EBSD detectors are easily available in various parts of the world,

as compared to TOF neutron diffractometers. This makes EBSD more useful today than any other technique for CPO analysis of rocks.

Summarily, any difference in the results obtained by means of the applied techniques is strictly related to specific factors that, depending on the nature of granitoid mylonite (i.e., polymineralic rock), should be accounted for: (a) quartz CPOs may be highly domainal—particularly where quartz ribbons anastomose around rigid feldspar clasts as revealed by pole figures related to the sub-areas depicted in Fig. 12; (b) microstructural and CPO complexities seen in 2D are likely to be more complex in 3D, making thus difficult to meaningfully compare CPOs essentially collected on 2D surfaces (optical microscope / universal stage and CIP methods) with CPO data collected in 3D (neutron diffraction method); and (c) statistical meaning of measured mineral CPOs (see also Table 2).

Application of quartz pole figures in structural geology

Quartz within the Montalto mylonites essentially consists of poly-crystalline aggregates derived from a recrystallization episode coeval with the Alpine metamorphic event and linked to the shear zone activity, which developed mineral parageneses (quartz, epidote, albitic feldspar, phengitic white mica, and chlorite) typical of greenschist to lower amphibolite facies conditions in the PT range 0.25–0.55 GPa and 350–550 °C (Cirrincione et al. 2008, 2009).

The quartz *c*-axis pole figures (Fig. 6) for samples M13, M8 and M3, show asymmetric *c*-axis concentration at high angles to the foliation normal, and it is likely that basal $\langle a \rangle$ is the dominant slip system and deformation occurred largely in simple shear (e.g., Schmid and Casey 1986). However, there is not much orientation of *a*-axes {11-20} (Fig. 8).

TOF data document a difference between pole figures of positive and negative rhombs that may be due to

mechanical Dauphiné twinning, aligning planes of positive rhombs perpendicular to the principal stress (e.g., Tullis 1970; Tullis and Tullis 1972; Pehl and Wenk 2005; Wenk et al. 2006, 2011; Menegon et al. 2011), or to activity of rhombohedral slip systems.

TOF results show a general tendency of a strong asymmetric *c*-maximum near to the *Z* direction especially for M13 and M8, suggesting dominant basal slip. In M3, and particularly in M4, the *c*-axis maximum is spreading into a girdle suggesting that possibly *c*-axes of dynamically recrystallized new grains have progressively rotated during deformation with respect to the host grains from which they nucleated, as demonstrated by poly-crystal plasticity simulations on similar rocks (Wenk et al. 1997). A single *c*-axis maximum near to *Z* is consistent with fabric patterns obtained from both experimentally and naturally sheared quartzite, showing extensive dynamic recrystallization under low temperature (Dell'Angelo and Tullis 1989, 1996) and greenschist facies conditions (Tagami and Takeshita 1998), respectively. Therefore, the observed *c*-axis maximum near to the *Z*-axis in the Montalto mylonites is possibly related to dynamically recrystallization under greenschist facies since soft orientations grew at the expenses of hard orientations for basal slip at large strains (Takeshita et al. 1999).

Central girdle in *c*-axis fabrics for samples M3 and M4 are oblique to both *X* (mineral lineation) and *Y* sample coordinates. Considering that the specimens were cut parallel to the most obvious mineral lineation, two interpretations can be made about such occurrence: (a) lineation is not a principal stretching direction (e.g., Lin and Williams 1992); (b) triaxial shear (rather than monoclinic shear) has occurred; (c) a combination of the above. According to a study on samples from the same area (Fazio et al. 2010), the first hypothesis could be the most probable because a hidden stretching lineation is overprinted by an intersection lineation which at places is the most evident at the outcrop scale.

Possibly, in the Montalto shear zone, as also indicated by the kinematic vorticity analysis (rigid grain net analysis) performed on feldspar porphyroclasts, a subsimple shear has developed (Fig. 4). The ultimate rock fabric should be then the result of a combination of simple shear and pure shear, for which relative percentages have been estimated to be in the intervals 30–40 and 60–70%, respectively (Fig. 4). It is difficult to establish whether the shear deformation switched during cyclic episodes, or maybe the coaxial strain has been subsequently overprinted by the non-coaxial one, which was likely dominant during the last exhumation phase coherently with the PT path proposed by Cirrincione et al. (2008) for these mylonitic rocks.

Conclusions

Comparison between quartz CPOs on granitoid mylonites from the Montalto shear zone (Calabria, southern Italy) by means of US, CIP, TOF and EBSD highlighted that each technique provides interesting information about grain population with respect to volume or area sizes taken into account.

Depending on the aim of the user and the goal of the investigation, we suggest that as a first approach, the universal stage (US) still has the advantage to depict a first-order representation of quartz *c*-axis distribution and permits operators to expeditiously answer many basic questions.

As a second step and/or for more detailed investigation, especially if a domain microstructural control is required, the CIP method is capable of providing good results with a strong control by the user. The main task of CIP is not to represent the textural features of the whole rock; instead, it focuses on understanding and interpreting chosen domains.

In order to provide a bulk textural crystallographic preferred orientation pattern of a specific mineral, TOF and EBSD have many advantages, most of which are related to the representativeness of information provided (Table 2). This especially holds for rocks characterized by fine grain size, as with ultramylonite sample M4 in this case (Fig. 12). Indeed, as also testified by RGN analysis (Fig. 4), the studied mylonite suite shows progressive grain size reduction with quartz average radii decreasing from 8–16 to 4–8 μm in samples M13 and M4, respectively (after Cirrincione et al. 2010). This makes it necessary to adopt an approach, which allows measurements on a large number of quartz grains, regardless of their size.

Quartz *c*-axis orientations collected on a suite of quartz-feldspar mylonites demonstrate that each method provides complementary results that are important for specific structural interpretations.

We deduce that the rocks involved in the syn-mylonitic exhumation stage of the Montalto shear zone developed a subsimple shear, as also suggested by shape analysis of feldspar porphyroclasts.

In conclusion, the user who wants to study naturally deformed rocks should first delineate particular strategies by taking into account the suggestions and considerations discussed in this paper.

Acknowledgements The authors are grateful to Renée Heilbronner for stimulating discussion made in the field and for helpful suggestions during image acquisition in Basel and subsequent notes. Authors also acknowledge with gratitude Kurt Mengel for EMPA analyses and for providing the Petmix facilities. We really appreciated suggestions by Richard Law, who significantly contributed to improve the clarity of an earlier version of the manuscript. Constructive review by Ali Faghih and fruitful suggestions of the Associate Editor Soumyajit

Mukherjee was really appreciated. We also thank critical review by an anonymous reviewer. HRW acknowledges access to the neutron scattering facilities of LANSCE at Los Alamos National Laboratory and help from Sven Vogel with data collections. He also is grateful for support from NSF (EAR-1343908) and DOE (DE-FG02-05ER15637). MAM acknowledges support provided by Indian Institute of Technology (IIT), Kharagpur (India), for carrying out EBSD analysis at its Central Research Facility (CRF) as a part of SG's MSc thesis work. Niloy Bhowmik of CRF (IIT Kharagpur) is thanked for helping with the EBSD analysis.

Appendix 1

For XRF analyses, glass disks were prepared of Lithium-tetra-borate and sample powder (<125 μm) which are mixed to a ratio of 6:1. A wave length-dispersive instrument (Panalytical Axios) was used for major element determination except hydrogen and carbon which together were determined as Loss on Ignition at 1150 $^{\circ}\text{C}$ (detection limit: 0.6 wt%). Accuracy is documented by repetitive analyses of international and in-house reference rocks and is better than 2% for elements Ca to Fe, better than 4% for elements from Al to K, and better than 6% for Na and Mg. Precision in the form of standard deviation is in the range of $\pm 2\%$ (rel.) for all major elements, except for loss on ignition, which is in the range of $\pm 5\%$ (rel.). Quantitative mineral analyses were done on a Cameca SX100 electron microprobe with 15 kV accelerating voltage and 20 nA beam current calibrated with natural mineral standards. Geochemical investigations were carried out at the Institut für Endlagerforschung, Clausthal University.

Appendix 2

For the CIP analysis, thin sections of approximately 25 μm thickness were prepared to ensure that quartz appears with a first-order gray color (Heilbronner 2010). This technique allows one to represent the *c*-axis position of each pixel with a characteristic color (Heilbronner and Barrett 2013), and pole figures were calculated from the azimuth and inclination images. Pictures were captured on a Zeiss polarization microscope using a Zeiss Axiocam-MRm monochromatic camera and a narrow band interference filter transmitting at 660 ± 9 nm (near infrared). By applying the CIP method, on each sample we have selected quartz domains following two fundamental criteria: (1) the grain size of quartz within the domain is representative of the entire thin section; (2) regions in the vicinity of large porphyroclasts which have a strong influence on the strain distribution in their surroundings were avoided. To prepare the CIP input, the freeware Image SXM software (Barrett

2008, <http://www.liv.ac.uk/~sdb/ImageSXM/>) was used. More details on the CIP method can be found elsewhere (Heilbronner 2000a, <http://www.unibas.ch/earth/micro/>). This filter renders interference colors as follows: first-order yellow as white, first-order red as gray and first-order blue as black. By inserting the filter, the interference colors (3 channels) are mapped uniquely into a gray value image (1 channel). The number of possible *c*-axis orientations for any given gray value is reduced with respect to the classical crossed polarizers conditions, but still there is no unique representation. If the quartz domain is acquired under so-called circular polarization conditions with crossed polarizers and two quarter wave length plate (1/4 lambda plates) inserted, these conditions yield an inclination image, where the grains appear dark if the *c*-axes are normal to the plane of the section, and white if the *c*-axes are parallel to it. Circular polarization is not sensitive to the azimuth of the *c*-axis. Grains which appear nearly white indicate that its *c*-axis lies very close to the plane of the section whereas black grains have a vertical *c*-axis. To map the two-dimensional orientation space, i.e., to uniquely color-code *c*-axis orientations, azimuth and inclination images are calculated and treated as two channels of a color image. Two-dimensional color look-up tables (CLUTs) are used to assign unique colors to any given pixel depending on the azimuth and inclination values of the *c*-axis at that point.

The standard input for CIP calculations consists of 18 rotation images, 2 tilt images and a circular polarization image (Heilbronner 2000b): the rotation images are a series of images with incremental relative rotation of the thin section with respect to the polarizers and the lambda plate (typically using a fixed interval of 10°), the tilt images are captured with the thin section tilted about the N–S and E–W axes. For the circular polarization image, crossed polarizers and two quarter-lambda plates (above and below the thin section) are used. Placing the input images in a stack (a multi-image sequence) and using macros, the images are registered (Heilbronner 2000b).

Additional images may be taken with parallel polarizers to obtain an image of dust and scratches for masking purposes, or one without the thin section in place in order to be able to correct uneven lighting.

Appendix 3

Nomenclature used in rigid grain net (RGN) analysis

W_m	Mean kinematic vorticity number
B^*	Shape factor
θ	Angle between clast long axis and macroscopic foliation
R	Porphyroclast aspect ratio (long axis/short axis)

- a* Major axis of the porphyroclast
b Minor axis of the porphyroclast

Equations used in the RGN calculations

$$\theta = 1/2 \sin^{-1} W_m/B^* \left\{ \left(1 - W_m^2\right)^{1/2} - \left(B^* - W_m^2\right)^{1/2} \right\}$$

$$B^* = (a^2 - b^2)/(a^2 + b^2).$$

References

- Anderson JL (1945) Deformation planes and crystallographic directions in quartz. *Geol Soc Am Bull* 56:409–430
- Baker DW, Wenk HR, Christie JM (1969) X-ray analysis of preferred orientation in fine-grained quartz aggregates. *J Geol* 77:143–172
- Barrett SD (2008) Image SXM. <http://www.ImageSXM.org.uk>
- Bestmann M, Kunze K, Matthews A (2000) Evolution of a calcite marble shear zone complex on Thassos Island, Greece: microstructural and textural fabrics and their kinematic significance. *J Struct Geol* 22:1789–1807
- Cirrincone R, Ortolano G, Pezzino A, Punturo R (2008) Poly-orogenic multi-stage metamorphic evolution inferred via P–T pseudosections: an example from Aspromonte Massif basement rocks (Southern Calabria, Italy). *Lithos* 103:466–502
- Cirrincone R, Fazio E, Fiannacca P, Ortolano G, Punturo R (2009) Microstructural investigation of naturally deformed leucogneiss from an Alpine shear zone (Southern Calabria–Italy). *Pure Appl Geophys* 166:995–1010
- Cirrincone R, Fazio E, Heilbronner R, Kern H, Mengel K, Ortolano G, Pezzino A, Punturo R (2010) Microstructure and elastic anisotropy of naturally deformed leucogneiss from a shear zone in Montalto (southern Calabria, Italy). *Geol Soc Lond Spec Publ* 332:49–68
- Cirrincone R, Fazio E, Ortolano G, Pezzino A, Punturo R (2012) Fault-related rocks: deciphering the structural–metamorphic evolution of an accretionary wedge in a collisional belt, NE Sicily. *Int Geol Rev* 54:940–956
- Cirrincone R, Fazio E, Fiannacca P, Ortolano G, Pezzino A, Punturo R, Romano V, Sacco V (2013) The Alpine evolution of the Aspromonte Massif: constraints for geodynamic reconstruction of the Calabria–Peloritani Orogen. *Geol Field Trips* 5:1–73. doi:10.3301/GFT.2013.01
- Cirrincone R, Fazio E, Fiannacca P, Ortolano G, Pezzino A, Punturo R (2015) The Calabria–Peloritani Orogen, a composite terrane in Central Mediterranean; its overall architecture and geodynamic significance for a pre-Alpine scenario around the Tethyan basin. *Period Mineral* 84:701–749
- de Araujo MNC, da Silva FCA, de Sá EFJ, Holcombe RJ, De Vasconcelos PM (2003) Microstructural evolution of the Serido' Belt, NE-Brazil: the effect of two tectonic events on development of *c*-axis preferred orientation in quartz. *J Struct Geol* 25:2089–2107
- Dell'Angelo LN, Tullis J (1989) Fabric development in experimentally sheared quartzites. *Tectonophysics* 169:1–21
- Dell'Angelo LN, Tullis J (1996) Textural and mechanical evolution with progressive strain in experimentally deformed aplite. *Tectonophysics* 256:57–82
- Dingley DJ (2004) Progressive steps in the development of electron backscatter diffraction and orientation imaging microscopy. *J Microsc* 213:214–224
- Duyster J (1996) StereoNett 2.0, University of Bochum. <http://homepage.ruhr-uni-bochum.de/Johannes.P.Duyster/stereo/stereoload.htm>
- Faghih A, Soleimani M (2015) Quartz *c*-axis fabric development associated with shear deformation along an extensional detachment shear zone: Chapedony Metamorphic Core Complex, Central-East Iranian Microcontinent. *J Struct Geol* 70:1–11
- Fazio E, Cirrincone R, Pezzino A (2008) Estimating P–T conditions of Alpine-type metamorphism using multistage garnet in the tectonic windows of the Cardeto area (southern Aspromonte Massif, Calabria). *Mineral Petrol* 93:111–142. doi:10.1007/s00710-007-0216-2
- Fazio E, Cirrincone R, Pezzino A (2009) Garnet crystal growth in sheared metapelites (southern Calabria–Italy): relationships between isolated porphyroblasts and coalescing euhedral crystals. *Period Mineral* 78:3–18. doi:10.2451/2009PM0001
- Fazio E, Punturo R, Cirrincone R (2010) Quartz *c*-axis texture mapping of mylonitic metapelite with rods structures (Calabria, southern Italy): clues for hidden shear flow direction. *J Geol Soc India* 75:171–182. doi:10.1007/s12594-010-0006-z
- Fazio E, Cirrincone R, Pezzino A (2015) Tectono-metamorphic map of the south-western flank of the Aspromonte Massif (southern Calabria–Italy). *J Maps* 11:85–100. doi:10.1080/17445647.2014.962634
- Fiannacca P, Lo Pò D, Ortolano G, Cirrincone R, Pezzino A (2012) Thermodynamic modeling assisted by multivariate statistical image analysis as a tool for unraveling metamorphic P–T–d evolution: an example from ilmenite-garnet-bearing metapelite of the Peloritani Mountains, southern Italy. *Mineral Petrol* 106:151–171
- Fiannacca P, Williams IS, Cirrincone R, Pezzino A (2013) The augen gneisses of the Peloritani Mountains (NE Sicily): granitoid magma production during rapid evolution of the northern Gondwana margin at the end of the Precambrian. *Gondwana Res* 23:782–796
- Frischbutter A, Neov D, Scheffzük C, Vrána M, Walther K (2000) Lattice strain measurements on sandstones under load using neutron diffraction. *J Struct Geol* 22:1587–1600
- Fuerten F (1997) A computer controlled rotating polarizer stage for the petrographic microscope. *Comput Geosci* 23:203–208
- Goodchild JS, Fuerten F (1998) Edge detection in petrographic images using the rotating polarizer stage. *Comput Geosci* 24:745–751
- Graessner T, Schenk V, Bröcker M, Mezger K (2000) Geochronological constraints on the timing of granitoid magmatism, metamorphism and post-metamorphic cooling in the Hercynian crustal cross-section of Calabria. *J Metamorph Geol* 18:409–421
- Heilbronner R (2000a) <http://www.unibas.ch/earth/micro/>
- Heilbronner R (2000b) Optical orientation imaging. In: Jessell MW, Urai JL (ed) Stress, strain and structure, a volume in honour of W D Means, vol 2, *Journal of the Virtual Explorer*
- Heilbronner R (2010) Mapping texture domains in quartzite microstructures. *J Geol Soc India* 75:160–170
- Heilbronner R, Barrett S (2013) Image analysis in earth sciences, microstructures and textures of earth materials. Springer, Berlin, Heidelberg
- Heilbronner R, Tullis J (2006) Evolution of *c*-axis pole figures and grain size during dynamic recrystallization: results from experimentally sheared quartzite. *J Geophys Res* 111:B10202. doi:10.1029/2005JB004194
- Hunter NJR, Hasalová P, Weinberg RF, Wilson CJL (2016) Fabric controls on strain accommodation in naturally deformed mylonites: the influence of interconnected micaceous layers. *J Struct Geol* 83:180–193

- Jeřábek P, Stünitz H, Heilbronner R, Lexa O, Schulmann K (2007) Microstructural-deformation record of an orogen-parallel extension in the Vepor Unit, West Carpathians. *J Struct Geol* 29:1722–1743
- Jessup MJ, Law RD, Frassi C (2007) The rigid grain net (RGN): an alternative method for estimating mean kinematic vorticity number (W_m). *J Struct Geol* 29:411–421
- Kepler R, Ullemeyer K, Behrmann JH, Stipp M, Kurzwski RM, Lokajčiček T (2015) Crystallographic preferred orientations of exhumed subduction channel rocks from the Eclogite Zone of the Tauern Window (Eastern Alps, Austria), and implications on rock elastic anisotropies at great depths. *Tectonophysics*. doi:10.1016/j.tecto.2015.02.011
- Kilian R, Heilbronner R, Stünitz H (2011) Quartz microstructures and crystallographic preferred orientation: which shear sense do they indicate? *J Struct Geol* 33:1446–1466
- Law RD (2014) Deformation thermometry based on quartz *c*-axis fabrics and recrystallization microstructures: a review. *J Struct Geol* 66:129–161
- Law RD, Schmid SM, Wheeler J (1990) Simple shear deformation and quartz crystallographic fabrics: a possible natural example from the Torridon area of NW Scotland. *J Struct Geol* 12:29–45
- Le Maitre RW (1979) A new generalised petrological mixing model. *Contrib Mineral Petrol* 71:133–137
- Leissa B, Ullemeyera K, Webera K, Brokmeier HG, Bungec HJ, Drury M, Faule U, ScheffzůĚkf CH, Weissa T, Waltherf K, Wenk HR (2000) Recent developments and goals in texture research of geological materials. *J Struct Geol* 22:1531–1540
- Lin S, Williams PF (1992) The geometrical relationship between the stretching lineation and the movement direction of shear zones. *J Struct Geol* 14:491–498
- Lister GS, Hobbs BE (1980) The simulation of fabric development during plastic deformation and its application to quartzite: the influence of deformation history. *J Struct Geol* 2:355–370
- Lutterotti L, Matthies S, Wenk HR, Schultz AJ, Richardson JW (1997) Combined texture and structure analysis of deformed limestone from time-of-flight neutron diffraction spectra. *J Appl Phys* 81:594–600
- Mainprice D, Bouchez JL, Blumenfeld P, Tubia JM (1986) Dominant *c* slip in naturally deformed quartz: implications for dramatic plastic softening at high temperature. *Geology* 14:819–822
- Matthies S, Pehl J, Wenk HR, Vogel S (2005) Quantitative texture analysis with the HIPPO TOF diffractometer. *J Appl Crystallogr* 38:462–475
- Menegon L, Piazolo S, Pennacchioni G (2011) The effect of Dauphiné twinning on plastic strain in quartz. *Contrib Mineral Petrol* 161:635–652
- Mukherjee S (2011) Mineral fish: their morphological classification, usefulness as shear sense indicators and genesis. *Int J Earth Sci* 100:1303–1314
- Mukherjee S (2012) Simple shear is not so simple! Kinematics and shear senses in Newtonian viscous simple shear zones. *Geol Mag* 149:819–826
- Mukherjee S (2013a) Deformation microstructures in rocks. Springer, Berlin, pp 1–111
- Mukherjee S (2013b) Channel flow extrusion model to constrain dynamic viscosity and Prandtl number of the Higher Himalayan Shear Zone. *Int J Earth Sci* 102:1811–1835
- Neumann B (2000) Texture development of recrystallised quartz polycrystals unravelled by orientation and misorientation characteristics. *J Struct Geol* 22:1695–1711
- Okudaira T, Takeshita T, Hara I, Ando J (1995) A new estimate of the conditions for transition from basal $\langle a \rangle$ to prism $\langle c \rangle$ slip in naturally deformed quartz. *Tectonophysics* 250:31–46
- Ortolano G, Cirrincione R, Pezzino A (2005) P-T evolution of Alpine metamorphism in the southern Aspromonte Massif (Calabria, Italy). *Schweiz Mineral Petrogr Mitteilungen* 85:31–56
- Panozzo-Heilbronner R, Pauli C (1993) Integrated spatial and orientation analysis of quartz *c*-axes by computer-aided microscopy. *J Struct Geol* 15:369–383
- Passchier CW, Trouw RAJ (2006) *Microtectonics*, 2nd edn. Springer, New York
- Pauli C, Schmid SM, Panozzo-Heilbronner R (1996) Fabric domains in quartz mylonites: localized three dimensional analysis of microstructure and texture. *J Struct Geol* 18:1183–1203
- Pehl J, Wenk HR (2005) Evidence for regional Dauphiné twinning in quartz from the Santa Rosa mylonite zone in Southern California. A neutron diffraction study. *J Struct Geol* 27:1741–1749
- Peternell M, Russell-Head DS, Wilson CJL (2011) A technique for recording polycrystalline structure and orientation during in situ deformation cycles of rock analogues using an automated fabric analyser. *J Microsc* 242:181–188
- Pezzano A, Pannucci S, Puglisi G, Atzori P, Ioppolo S, Lo Giudice A (1990) Geometry and metamorphic environment of the contact between the Aspromonte-Peloritani Unit (Upper Unit and Madonna dei Polsi Unit (Lower Unit) in the central Aspromonte area (Calabria). *Boll Soc Geol Ital* 109:455–469
- Pezzano A, Angi G, Fazio E, Fiannacca P, Lo Giudice A, Ortolano G, Punturo R, Cirrincione R, De Vuono E (2008) Alpine metamorphism in the Aspromonte Massif: implications for a new framework of the southern sector of the Calabria–Peloritani Orogen (Italy). *Int Geol Rev* 50:423–441
- Phillips WR (1971) *Mineral optics: principles and techniques*. W.H. Freeman and Company, San Francisco, p 249
- Price GP (1973) The photometric method in microstructural analysis. *Am J Sci* 273:523–537
- Prior DJ, Boyle AP, Brenker F, Cheadle MC, Day A, Lopez G, Peruzzo L, Potts GJ, Reddy S, Spiess R, Timms NE, Trimby P, Wheeler J, Zetterstrom L (1999) The application of electron backscatter diffraction and orientation contrast imaging in the SEM to textural problems in rocks. *Am Mineral* 84:1741–1759
- Prior DJ, Mariani E, Wheeler J (2009) EBSD in the earth sciences: applications, common practice and challenges. In: Schwartz AJ, Kumar M, Adams BL, Field DP (eds) *Electron backscatter diffraction in materials science*, 2nd edn. Springer, New York, pp 345–360
- Punturo R, Cirrincione R, Fazio E, Fiannacca P, Kern H, Mengel K, Ortolano G, Pezzino A (2014) Microstructural, compositional and petrophysical properties of mylonitic granodiorites from an extensional shear zone (Rhodope Core complex, Greece). *Geol Mag* 151:1051–1071. doi:10.1017/S001675681300109X
- Ree JH (1994) Grain boundary sliding and development of grain boundary openings in experimentally deformed octachloropropane. *J Struct Geol* 16:403–418
- Renjith AR, Mamtani MA (2014) Domainal petrofabric analysis of micaceous quartzite using EBSD data: role of muscovite in LPO evolution of quartz. *J Geol Soc India* 83:479–482
- Renjith AR, Mamtani MA (2015) Integrating EBSD and magnetic susceptibility data to decipher intensity of SPO and strain in deformed quartzite. EBSD Application Note-2015, Oxford Instruments. (www.oxinst.com/ebds)
- Renjith AR, Mamtani MA, Urai JL (2016) Fabric analysis of quartzites with negative magnetic susceptibility—does AMS provide information of SPO or CPO of quartz? *J Struct Geol* 82:48–59
- Sander B (1930) *Gefügekunde der Gesteine*. Springer, Wien
- Sander B (1950) *Einführung in die Gefügekunde der geologischen Körper, Band II: Die Korngefüge*. Springer, Wien

- Schmid SM, Casey M (1986) Complete fabric analysis of some commonly observed quartz c-axis patterns. In: Heard HC, Hobbs BE (ed) *Mineral and rock deformation: laboratory studies* (the Paterson volume). American Geophysical Union Geophysical Monograph 36:263–286
- Schmidt W (1925) Gefügestatistik. *Tschermaks Mineral Petrogr Mitt* 38:342–423
- Sengupta N, Mukhopadhyay D, Sengupta P, Hoffbauer R (2005) Tourmaline-bearing rocks in the Singhbhum shear zone, Eastern India: evidence of boron infiltration during regional metamorphism. *Am Mineral* 90:8–9
- Stipp M, Stünitz H, Heilbronner R, Schmid SM (2002) The eastern Tonale fault zone: a “natural laboratory” for crystal plastic deformation of quartz over a temperature range from 250 to 700 °C. *J Struct Geol* 24:1861–1884
- Tagami M, Takeshita T (1998) c-axis fabrics and microstructures in quartz schist from the Sambagawa metamorphic belt, central Shikoku, Japan. *J Struct Geol* 20:1549–1568
- Takeshita T, Wenk HR, Lebensohn R (1999) Development of preferred orientation and microstructure in sheared quartzite: comparison of natural data and simulated results. *Tectonophysics* 312:133–155
- Thomson SN (1994) Fission track analysis of the crystalline basement rocks of the Calabrian Arc, southern Italy: evidence of Oligo–Miocene late-orogenic extension and erosion. *Tectonophysics* 238:331–352
- Tullis J (1970) Quartz: preferred orientation in rocks produced by Dauphiné twinning. *Science* 168:1342–1344
- Tullis J, Tullis TE (1972) Preferred orientation produced by mechanical Dauphiné twinning. *Thermodynamics and axial experiments*. *Am Geophys Union Geophys Monogr* 16:67–82
- van Daalen M, Heilbronner R, Kunze K (1999) Orientation analysis of localized shear deformation in quartz fibres at the brittle–ductile transition. *Tectonophysics* 303:83–108
- Wenk HR, Canova G, Brechet Y, Flandin L (1997) A deformation-based model for recrystallization of anisotropic materials. *Acta Mater* 45:3283–3296
- Wenk HR, Lutterotti L, Vogel S (2003) Texture analysis with the new HIPPO TOF diffractometer. *Nucl Instrum Methods Phys Res Sect A* 515:575–588
- Wenk HR, Leonardelli I, Rybacki E, Dresen G, Barton N, Franz H, Gonzalez G (2006) Dauphiné twinning and texture memory in polycrystalline quartz. Part 1: experimental deformation of novaculite. *Phys Chem Miner* 33:667–676
- Wenk HR, Lutterotti L, Vogel S (2010) Rietveld texture analysis from TOF neutron diffraction data. *Powder Diffr* 25:283–296
- Wenk HR, Janssen C, Kenkmann T, Dresen G (2011) Mechanical twinning in quartz: shock experiments, impact, pseudotachylites and fault breccias. *Tectonophysics* 510:69–79
- Wenk HR, Vasin RN, Kern H, Matthies S, Vogel SC, Ivankina TI (2012) Revisiting elastic anisotropy of biotite gneiss from the Outokumpu scientific drill hole based on new texture measurements and texture-based velocity calculations. *Tectonophysics* 570–571:123–134
- Wilkinson AJ (1999) Introduction. *J Microsc* 195:169. doi:[10.1046/j.1365-2818.1999.00626.x](https://doi.org/10.1046/j.1365-2818.1999.00626.x)
- Wilson CJ, Russell-Head DS, Kunze K, Viola G (2007) The analysis of quartz c-axis fabrics using a modified optical microscope. *J Microsc* 227:30–41
- Wright SI, Nowell MM, Field DP (2011) A Review of strain analysis using electron backscatter diffraction. *Microsc Microanal* 17:316–329. doi:[10.1017/S1431927611000055](https://doi.org/10.1017/S1431927611000055)